Magnetic, transport, and thermal properties of the half-Heusler compounds ErPdSb and YPdSb

K. Gofryk,[1,2] D. Kaczorowski,[1] T. Plackowski,[1] J. Mucha,[1] A. Leithe-Jasper,[3] W. Schnelle,[3] and Yu. Grin[3]
[1]*Institute of Low Temperature and Structure Research, Polish Academy of Sciences, P.O. Box 1410, 50-950 Wrocław, Poland*
[2]*Institute for Transuranium Elements, European Commission Joint Research Centre, Postfach 2340, 76125 Karlsruhe, Germany*
[3]*Max-Planck-Institut für Chemische Physik fester Stoffe, Nöthnitzer Strasse 40, 01187 Dresden, Germany*
(Received 10 January 2007; revised manuscript received 26 February 2007; published 22 June 2007)

The half-Heusler compounds ErPdSb and YPdSb were studied by means of x-ray diffraction, magnetic susceptibility, electrical resistivity, magnetoresistivity, thermoelectric power, Hall effect, thermal conductivity, and specific heat measurements, performed in the temperature range 1.5–300 K and in magnetic fields up to 12 T. The Er-based compound is a paramagnet down to 1.7 K and shows localized magnetism of Er^{3+} ions, while YPdSb exhibits a weak diamagnetic behavior. The crystal field effect in ErPdSb brings about a distinct Schottky anomaly in the specific heat. The total splitting of the erbium $^4I_{15/2}$ multiplet in a cubic crystal field potential is of the order of 200 K, with a doublet being the ground state. Electrical properties of ErPdSb and YPdSb are governed by the formation of narrow gaps in the electronic band structures very close to the Fermi level. The Hall effect measured for ErPdSb indicates a complex electronic structure with multiple electron and hole bands with different temperature and magnetic field variations of carrier concentrations and mobilities. The thermal conductivity of ErPdSb is relatively low and dominated by the phonon contribution. At room temperature the Seebeck coefficient is of order 150 μV/K for Er- and 200 μV/K for Y-based compound, respectively, making these materials promising candidates for thermoelectric applications. This conjecture is supported by the value of the figure of merit of ErPdSb, which is about 0.15 at room temperature.

DOI: 10.1103/PhysRevB.75.224426 PACS number(s): 71.20.Eh, 71.55.Ak, 72.15.Eb, 72.15.Jf

I. INTRODUCTION

The half-Heusler phases of general composition *XYZ*, where *X* and *Y* stand for *d*- or *f*-electron transition metals, respectively, and *Z* denotes a *p*-electron element, crystallize with the cubic MgAgAs type of structure (space group $F\bar{4}3m$). They continuously attract much attention due to their remarkable physical properties,[1] e.g., a wide variety of magnetic and electrical transport behavior including the heavy fermion state,[2–5] shape memory effect,[6] giant magnetoresistance,[7,8] half-metallic ferromagnetism,[9] and semimetallic or semiconducting behavior.[10] In systems like *X*NiSn (*X*=Ti,Hf,Zr),[11–13] the presence of vacancies sometimes leads to the formation of a narrow gap in the density of electronic states near the Fermi level. Because of that these compounds usually exhibit large magnitudes of the thermoelectric power, which together with their relatively low electrical resistivity makes them promising materials for thermoelectrical applications.[14–20]

In the course of systematic investigations of 4*f*-electron-based half-Heusler phases we have already briefly reported on the physical properties of a few ternaries with the composition *R*PdSb and RPdBi where *R* is a rare earth element .[21,22] Here, we give a full account of our studies on the low-temperature behavior of the erbium-based antimonide ErPdSb, as well as on its isostructural analog YPdSb, which does not contain 4*f* electrons. In the following we summarize the results of magnetic, electrical transport (resistivity, thermoelectric power, Hall effect), thermal transport, and heat capacity measurements, all performed on high-quality polycrystalline samples of the two ternaries. The transport data on ErPdSb complete those reported very recently by Sekimoto *et al.*[23] which span the high-temperature region from 300 to 1000 K. From the latter data ErPdSb was characterized as a semiconductor with an energy gap of 0.28 eV, which brings about rather high values of the thermoelectric power factor above room temperature (exceeding 10 μW K^{-2}), and an enhanced magnitude of the dimensionless figure of merit, which reaches 0.16 near 700 K.

II. EXPERIMENTAL DETAILS

Polycrystalline samples of ErPdSb and YPdSb were prepared by arc-melting the constituents (*R* 99.9 wt %, Pd 99.999 wt %, Sb 99.999 wt %) under argon atmosphere. The ingots were then wrapped in tantalum foil, sealed in evacuated quartz tubes, and annealed at temperatures 950 and 700 °C for ErPdSb and YPdSb, respectively, for several weeks. The quality of the obtained materials was checked at room temperature by powder x-ray diffraction (Huber Guinier G670 image plate camera with Cu $K\alpha_1$ radiation, λ =1.5406 Å, and LaB_6 as internal standard, a=4.15692 Å), energy-dispersive x-ray spectroscopy (EDXS) analysis [Philips XL30 scanning electron microscope with integrated EDXS system and S-UTW-Si-(Li) detector] and optical metallography (Zeiss Axioplan 2 optical microscope with a charge-coupled device camera).

Magnetization measurements were carried out in the temperature range 1.7–300 K and in magnetic fields up to 5 T using a superconducting quantum interference device (SQUID) magnetometer (Quantum Design MPMS-5). The electrical resistivity was measured from 4.2 to 300 K by a four-point dc technique. Magnetoresistivity measurements were made in fields up to 8 T. The thermoelectric power was measured from 6 to 300 K employing a differential method with copper as a reference material. Hall effect measurements were performed within the temperature range 1.5–300 K and in applied fields up to 13 T (Oxford Instru-

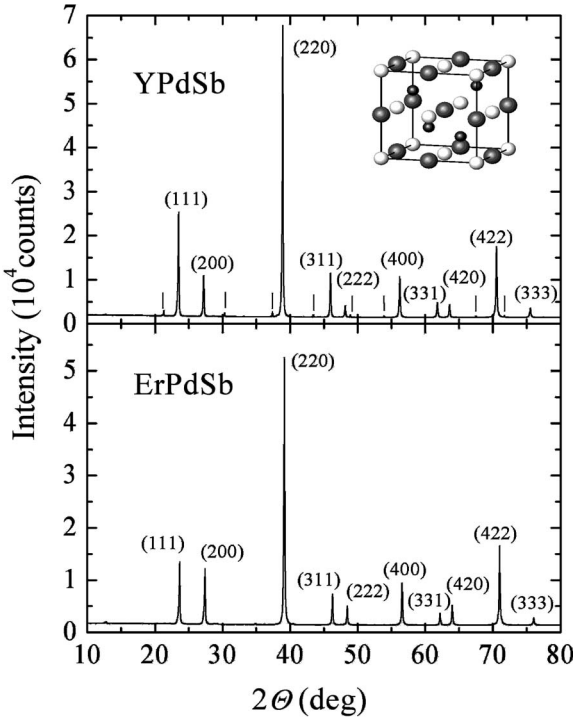

FIG. 1. Powder diffraction patterns of YPdSb and ErPdSb. For YPdSb the small vertical ticks indicate peaks coming from LaB_6, which was used as a standard. The inset shows the crystal structure of the MgAgAs type. Large gray spheres, *R* atoms; small black spheres, Pd atoms; white spheres, Sb atoms.

ments Teslatron). The thermal conductivity was measured from 6 to 300 K using a steady-state method implemented into a bath cryostat with a setup similar to that described in Ref. 24. Heat capacity experiments were performed within the temperature range 1.8–300 K and in magnetic fields up to 9 T by a relaxation method employing a Quantum Design PPMS-9 platform.

III. RESULTS AND DISCUSSION

A. Sample characterization

The powder x-ray diffraction patterns of the compounds studied were fully indexed within cubic face-centered unit cells with the lattice parameters $a=6.5316(3)$ Å for YPdSb and $a=6.4973(3)$ Å for ErPdSb (see Fig. 1). These values are close to those reported in the literature.[25] Comparison of the experimental and calculated intensities of the diffraction peaks confirmed unambiguously that the crystal structures of both phases belong to the MgAgAs type [space group $F\bar{4}3m$, 4Y (Er) at 4(*c*) $\frac{1}{4}\frac{1}{4}\frac{1}{4}$, 4Pd at 4(*a*) 000 and 4Sb at 4(*d*) $\frac{3}{4}\frac{3}{4}\frac{3}{4}$]. Detailed analysis of the x-ray diffraction data did not reveal reflections of any spurious phases in the samples. Some traces of minority phases (mainly YPd_3 and $ErPd_3$) could only be found by optical metallography (cf. Fig. 2). The chemical compositions of the samples determined from the EDXS data are $Y_{31.0(2)}Pd_{33.7(1)}Sb_{35.3(2)}$ and $Er_{34.2(1)}Pd_{32.6(1)}Sb_{33.2(3)}$. Whereas the composition of the Er-based phase is very close to the ideal one (ErPdSb), the Y-containing compound shows small deviation from the ideal composition, yielding the exact formula $Y_{1-x}PdSb_{1+x}$ with $x \approx 0.03$, thus suggesting some occupational disorder on the crystallographic sites of the Y and Sb atoms.

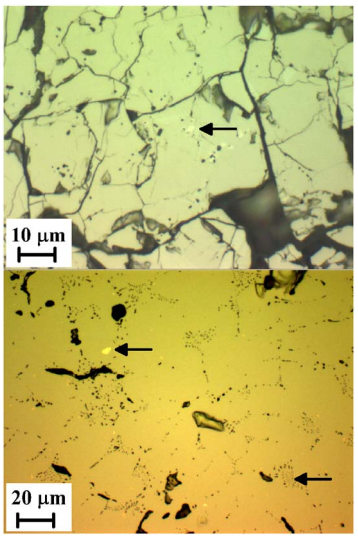

FIG. 2. (Color online) Microphotographs of the $Y_{1-x}PdSb_{1+x}$ (top) and ErPdSb (bottom) samples. The majority phases form large grains. Some grains of the minority phases are indicated by the arrows.

B. Magnetic properties

The temperature dependence of the inverse magnetic susceptibility of ErPdSb is shown in Fig. 3(a). Above 60 K the $\chi^{-1}(T)$ curve follows a Curie-Weiss law with the effective magnetic moment $\mu_{\text{eff}}=9.43\mu_B$, which is very close to the theoretical Hund's rule value for Er^{3+} ions $\{g[J(J+1)]^{1/2}=9.59\}$. The paramagnetic Curie temperature is small and negative ($\Theta_p=-4.2$ K), thus indicating weak electronic correlations of antiferromagnetic nature. The small deviation of the $\chi^{-1}(T)$ curve from the linear behavior occurring at low temperatures is probably due to the crystal field effect.

The low-temperature dependencies of the magnetic susceptibility measured at several different magnetic fields are displayed in Fig. 3(b). Up to 1 T, the susceptibility is field independent and shows no hint of any magnetic ordering above 1.7 K. In stronger magnetic fields some flattening of $\chi^{-1}(T)$ on lowering the temperature is observed. This feature corresponds to a Brillouin-like curvature of the field variation of the magnetization below 10 K, as displayed in the inset to Fig. 3(a). At 1.7 K the magnetic moment measured in a field of 5 T is $6.2\mu_B$/Er atom, which is a strongly reduced value with respect to that calculated for the free Er^{3+} ion ($gJ=9$). This finding clearly indicates splitting of the ground multiplet $^4I_{15/2}$ in a cubic crystal field potential.

For YPdSb the magnetic measurements have revealed hardly any temperature dependence of the molar magnetic susceptibility, which at room temperature amounts to about -90×10^{-6} emu mol^{-1}. At 1.72 K the magnetization shows a linear negative response to the applied magnetic field. Both

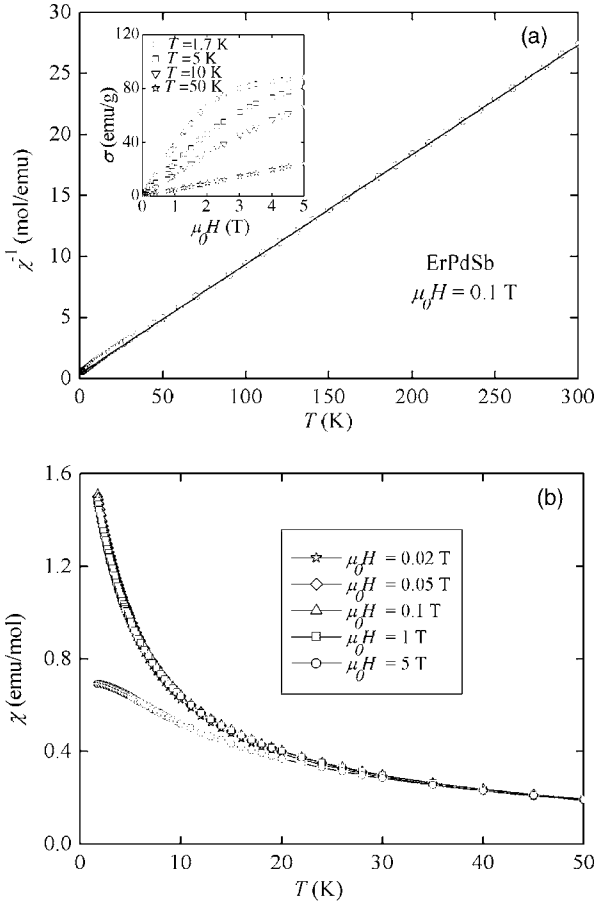

FIG. 3. (a) Temperature dependence of the inverse magnetic susceptibility of ErPdSb. The solid line is the least-squares fit of the experimental data to the Curie-Weiss law. Inset: Field dependence of the magnetization taken at several different temperatures. (b) Low-temperature susceptibility measured in different magnetic fields.

these findings clearly indicate that YPdSb is a weak diamagnet.

C. Heat capacity

Figure 4 shows the temperature dependencies of the specific heat of ErPdSb and YPdSb. Both C_p curves have a typical sigmoidlike shape and approach at high temperatures a value expected from the Dulong-Petit law, i.e., $C_p = 3nR = 74.8$ J mol^{-1} K^{-1}, where n is the number of atoms per molecule and R is the gas constant. At low temperatures the specific heat of ErPdSb forms an upturn (see discussion below), whereas that of the Y-based compound gradually diminishes to zero. Below $T \approx 10$ K the $C_p(T)$ variation of YPdSb can be well described (see the inset to Fig. 4) by the formula

$$C_p(T) = \gamma T + \beta T^3, \tag{1}$$

with the coefficients $\gamma = 0.2$ mJ mol^{-1} K^{-2} and $\beta = 0.28$ mJ mol^{-1} K^{-4}. The electronic contribution to the specific heat is very small, in accordance with the semiconductinglike behavior of the resistivity of YPdSb (cf. Sec. III D).

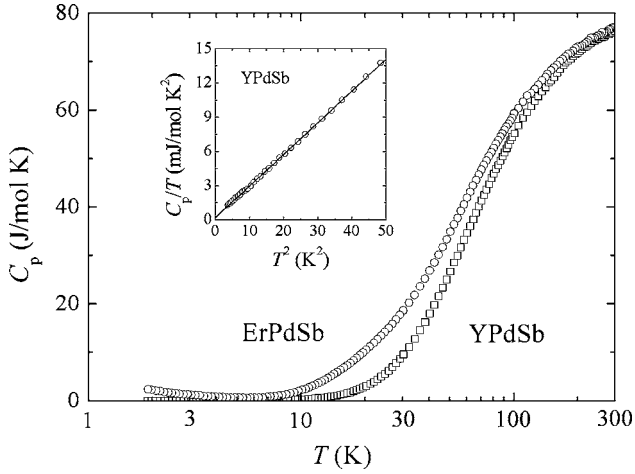

FIG. 4. Temperature dependencies of the specific heat of ErPdSb and YPdSb in a semilogarithmic representation. The inset presents the low-temperature data of YPdSb as a C_p/T vs T^2 function. The solid line is the least-squares fit according to Eq. (1).

From the value of β one estimates the Debye temperature $\Theta_D = (12R\pi^4 n/5\beta)^{1/3}$ to be about 275 K. This result confirms the value of $\Theta_D = 263$ K given in Ref. 23, which was calculated from the longitudinal and shear sound velocities measured for ErPdSb at room temperature by an ultrasonic method.

Bearing in mind that Eq. (1) is valid for temperatures $T < \Theta_D/20$ only, in order to describe the temperature variation of the specific heat of YPdSb in a wider temperature range one should apply the expression[26]

$$C_p(T) = \gamma T + (1-k)C_D(T) + kC_E(T), \tag{2}$$

in which the lattice contribution to the specific heat is accounted for by considering both the Debye function

$$C_D(T) = 9nR\left(\frac{T}{\Theta_D}\right)^3 \int_0^{\Theta_D/T} \frac{x^4 \exp(x)}{[\exp(x)-1]^2} dx \tag{3}$$

and the Einstein function

$$C_E(T) = 3nR\left(\frac{\Theta_E}{T}\right)^3 \left[\exp\left(\frac{\Theta_E}{T}\right) - 1\right]^{-2} \exp\left(\frac{\Theta_E}{T}\right) \tag{4}$$

with the k parameter ensuring the proper quantity of the oscillator modes involved. The least-squares fit of this formula to the experimental data below 100 K (see Fig. 5) yields the following parameters: $\gamma = 0.3$ mJ mol^{-1} K^{-2}, $\Theta_D = 270$ K, $\Theta_E = 110$ K, and $k = 0.08$. It is worthwhile noting that the values of the Sommerfeld coefficient and the Debye temperature are very close to those obtained from Eq. (1). Apparently, the Einstein term gives only a small contribution to the total specific heat of YPdSb (cf. the very small value of k) and the latter is clearly dominated by the Debye term (cf. Fig. 5). Nevertheless, as displayed in the inset to Fig. 5, the Einstein contribution is not negligible and brings about a distinct maximum in the C_p/T^3 vs T plot at a temperature $\Theta_{max} = 23$ K that scales very well with the Einstein temperature derived from Eq. (2) [$\Theta_E \approx 5\Theta_{max}$ (Ref. 27)].

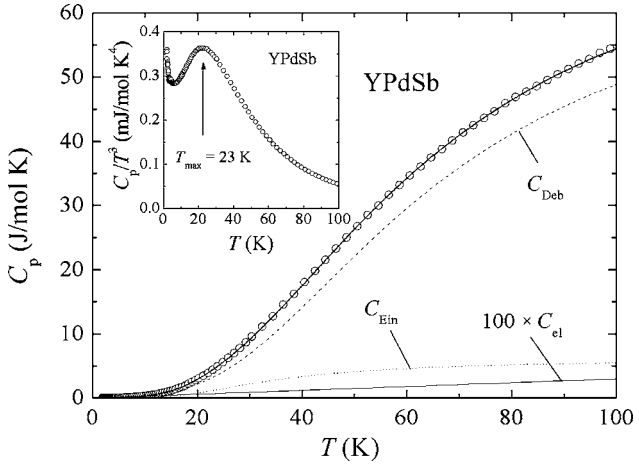

FIG. 5. Temperature variation of the specific heat of YPdSb below 100 K. The thick solid line is the fit of Eq. (2) to the experimental data. The dashed, dotted, and thin solid curves represent the Debye, Einstein, and electronic (for the sake of clarity multiplied by 100) contributions, respectively. The inset shows the specific heat data in the form of a C_p/T^3 vs T plot.

In order to estimate the magnetic contribution ΔC to C_p of ErPdSb one may assume that the phonon contribution to the total specific heat is as that in the isostructural counterpart YPdSb. Moreover, because of similar semiconductinglike conductivity in both compounds (see Sec. III D), it seems reasonable that the Sommerfeld coefficient in ErPdSb is as small as that in YPdSb. With these assumptions ΔC is given by $\Delta C = C_p^{\mathrm{ErPdSb}} - C_p^{\mathrm{YPdSb}}$, as shown in Fig. 6. The overall shape of the $\Delta C(T)$ curve with a pronounced maximum near 30 K suggests a predominant contribution due to the crystalline electric field (CEF). In a cubic crystal field potential the $^4I_{15/2}$ multiplet of the Er^{3+} ion splits into three quartets and two doublets.[28] Thus the ΔC data were analyzed in terms of the general expression for a Schottky anomaly,[27]

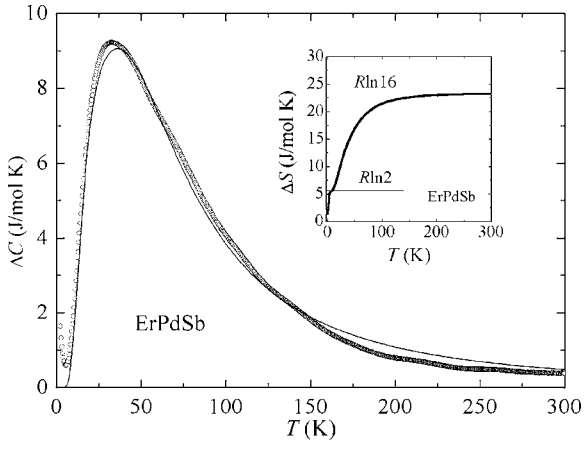

FIG. 6. Temperature dependence of the magnetic contribution to the specific heat of ErPdSb. The solid line is the fit of Eq. (5) to the experimental data with the parameters given in the text. The inset displays the temperature variation of the magnetic entropy normalized to the value expected at 300 K for the entire $^4I_{15/2}$ multiplet.

$$\Delta C(T) = \frac{R}{ZT^2}\sum_i g_i \Delta_i^2 \exp\left(-\frac{\Delta_i}{T}\right) - \frac{R}{Z^2T^2}\left[\sum_i g_i \Delta_i \exp\left(-\frac{\Delta_i}{T}\right)\right]^2 \quad (5)$$

where Z is the partition function

$$Z = \sum_i g_i \exp\left(-\frac{\Delta_i}{T}\right), \quad (6)$$

and Δ_i and g_i stand for the energy and the degeneracy of the respective crystal field levels, respectively. For $i=1,\ldots,5$ and $g_i=2$ or 4 (Kramers ion), appropriate for the case of ErPdSb, one obtains a very good description of the $\Delta C(T)$ curve (above 10 K) for the following CEF scheme: doublet-quartet-doublet with the energies $\Delta_1=0$ K, $\Delta_2=61$ K, and $\Delta_3=114$ K, and the other two excited quartets treated as a pseudodegenerate state located at 186 K above the ground state. The total CEF splitting derived in this way is similar to that found by inelastic neutron scattering for a closely related half-Heusler phase ErNiSb.[29] In the latter case, however, the order of crystal field levels is reversed compared to that in ErPdSb, with a quartet being the ground state, and a set of quartet, doublet, quartet, and doublet being the successive excited levels located at 92, 108, 166, and 220 K above the ground level, respectively.[29]

The presence of the doublet CEF ground state in ErPdSb is corroborated by a magnetic entropy analysis. In the inset to Fig. 6 the temperature dependence of the entropy gain is shown, calculated from the $\Delta S(T)$ data from 1.8 up to 300 K, yet shifted upward in such a way as to fix the room temperature value of ΔS at $R \ln 16$, corresponding to the 16-fold degeneracy of the $^4I_{15/2}$ multiplet. This handling of the data is justified by the presence of an extended plateau in $\Delta S(T)$ below 300 K down to about 180 K, which indicates hardly any crystal field effect in this range, in perfect agreement with the Schottky effect analysis and the Curie-Weiss behavior of the magnetic susceptibility. Then, another small plateau in $\Delta S(T)$ is seen at low temperatures at a value of $R \ln 2$, corresponding to a doubly degenerate ground state.

An unusual feature in the specific heat of ErPdSb, hitherto not discussed, is the upturn of the C_p curve below 6 K. It is hardly plausible that it arises due to a magnetic phase transition because the magnetic susceptibility is featureless down to 1.7 K (see Fig. 3). On the other hand, the character of this anomaly with C_p being proportional to T^{-2} is reminiscent of a Schottky effect (see the inset to Fig. 7). Essentially it might be due to a nuclear contribution to the specific heat; however, the relatively high temperature it is seen at makes also this hypothesis unlikely. Therefore, in order to clarify the nature of the low-temperature specific heat of ErPdSb, it was measured in several different applied magnetic fields. The results of these studies are shown in Fig. 7 in the form of a C_p/T vs T plot. Apparently, with increasing field the upturn shifts to higher temperatures and transforms into a maximum, which gradually broadens and diminishes its magnitude with further

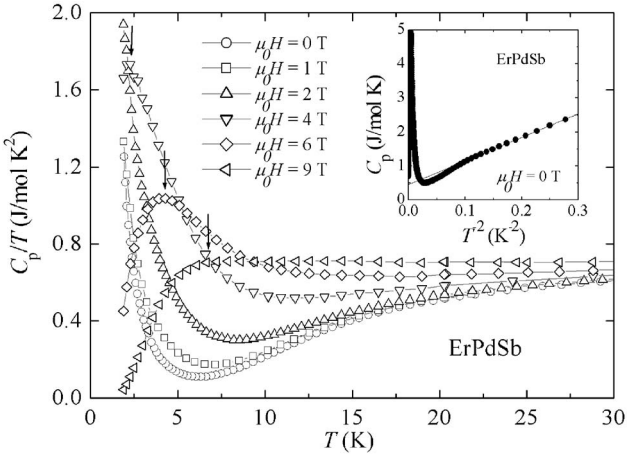

FIG. 7. Low-temperature dependencies of the specific heat over temperature ratio of ErPdSb taken at several magnetic fields. The arrows indicate the positions T_{max} of maxima in C_p/T. The inset presents the zero-field specific heat data in the form C_p vs T^{-2}.

rising field. Such a behavior indeed resembles that expected for a degenerate ground state split due to the Zeeman effect in internal and external magnetic fields.

D. Transport properties

1. Electrical resistivity

Figure 8 presents the temperature dependence of the electrical resistivity of YPdSb. It is quite large, of the order of several mΩ cm, and exhibits semiconductinglike behavior in the entire temperature range studied. As shown by the dashed line in Fig. 8 the resistivity may be quite well reproduced by a simple conduction model that involves two parallel conduction channels: one corresponding to thermal activation of the carriers over a small energy gap E_g and the second one related to variable range hopping processes quantified by the

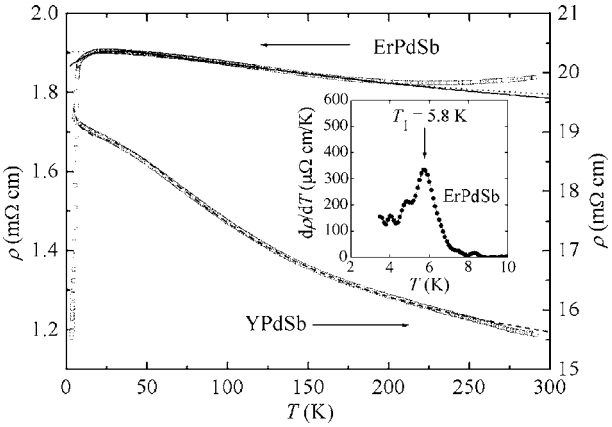

FIG. 8. Temperature dependencies of the electrical resistivity of YPdSb and ErPdSb. For YPdSb the dashed line represents the fit of the experimental data to Eq. (7). For ErPdSb the dotted and the solid lines are least-square fits of the experimental data to Eqs. (8) and (9), respectively. Inset: Low-temperature variation of the temperature derivative of the resistivity of ErPdSb.

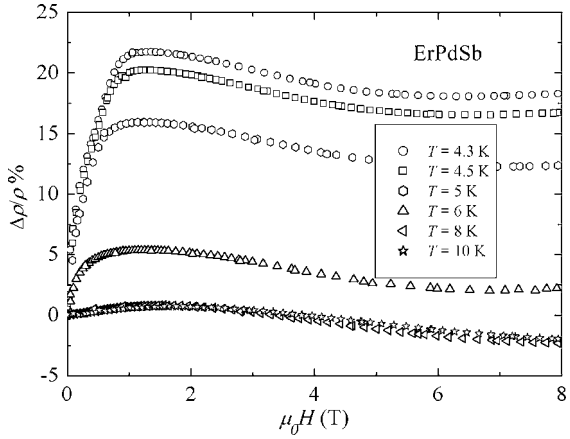

FIG. 9. Magnetic field variations of the transverse magnetoresistivity of ErPdSb below 10 K.

Mott temperature T_M that is related to the localization energy. Within this approach the resistivity is given by the formula

$$\frac{1}{\rho(T)} = \sigma_{act} \exp\left(\frac{-E_g}{2k_BT}\right) + \sigma_{hop}\left[\exp\left(\frac{T_M}{T}\right)\right]^{-1/4}. \quad (7)$$

Fitting Eq. (7) to the experimental data of YPdSb yields the parameters: $\sigma_{act}=5.3\times10^{-5}$ $(\mu\Omega\ \text{cm})^{-1}$, $\sigma_{hop}=1.75\times10^{-4}$ $(\mu\Omega\ \text{cm})^{-1}$, $E_g=25.3$ meV, and $T_M=0.6$ K. The Mott temperature obtained for YPdSb is similar to the T_M previously observed in the TbNiSb and HoNiSb half-Heusler compounds.[7]

The resistivity of ErPdSb is about one order of magnitude smaller than that of the Y-based compound, and its temperature variation is considerably different. On cooling the specimen from room temperature, the resistivity first slightly decreases, goes through a shallow minimum near 220 K, and then rises only very modestly to reach a maximum value of about 1.8 mΩ cm at $T_{max}=20$ K, which is eventually followed by a very rapid drop below 6 K. The latter anomaly manifests itself as a pronounced kink in the temperature dependence of derivative of the resistivity $d\rho/dT$ (see the inset to Fig. 8).

In this low-temperature region $\rho(T)$ is strongly dependent on an applied magnetic field. Figure 9 shows the transverse magnetoresistivity (i.e., the magnetic field is applied perpendicular to the direction of the electrical current), defined as $\Delta\rho/\rho=[\rho(B)-\rho(B=0)]/\rho(B=0)$, measured as a function of the magnetic field strength. Below 6 K one observes a distinct rise of the magnetoresistivity up to a field of about 1.5 T, above which the magnitude of $\Delta\rho/\rho$ smoothly diminishes, showing some tendency to saturate in fields stronger than 5 T. At $T=4.3$ K the magnetoresistivity reaches a maximum value of about 22%. At higher temperatures this value gradually decreases and the maximum in $\Delta\rho/\rho$ broadens considerably, yet the shape of the isotherms on the high-field side hardly changes (note that the magnetoresistivity curves are nearly parallel to each other). A distinctly different behavior of the magnetoresistivity is observed above 6 K. In this temperature range $\Delta\rho/\rho$ shows very small positive val-

ues in fields below about 4 T and turns over to negative ones in stronger fields. In 8 T the magnetoresistivity measured at 10 K amounts to about −2.5% only.

The unusual low-temperature behavior of the resistivity of ErPdSb is discussed in Ref. 21. Above 6 K the general shape of $\rho(T)$ recalls the electrical conductivity characteristics of semimetals or strongly doped semiconductors.[30] Indeed, above T_{max} the experimental data can be well approximated by the formula

$$\frac{1}{\rho(T)} = \sigma_a + b \exp\left(\frac{-E_g}{2k_B T}\right), \tag{8}$$

which accounts for excitation of conduction electrons over an energy gap E_g. The parameters derived by least-squares fitting of this equation in the range 20–200 K are as follows: $\sigma_a = 5.3 \times 10^{-4}$ $(\mu\Omega\ \mathrm{cm})^{-1}$, $b = 6.05 \times 10^{-5}$ $(\mu\Omega\ \mathrm{cm})^{-1}$, and $E_g = 34$ meV. In order to describe the thermal dependence of the resistivity of ErPdSb in a broader temperature range, a simple model of the electronic band structure of small gap semiconductors may be used, similar to that applied in Refs. 21 and 22 to the $\rho(T)$ variations of the half-Heusler compounds HoPdSb, DyPdBi, and ErPdBi. In this approach the resistivity varies as

$$\rho(T) = \frac{n_0 \rho_0 + \rho_{ph}(T)}{n(T)}, \tag{9}$$

where ρ_0 is the residual resistivity, n_0 stands for the number of charge carriers at $T=0$, $n(T)$ denotes the temperature-dependent total number of carriers, and $\rho_{ph}(T)$ represents scattering of carriers by phonons. For temperatures above $\Theta_D/10$, $\rho_{ph}(T)$ can by approximated by the function $\rho_{ph}(T) = c_{ph}T$. The best fit of Eq. (9) to the experimental data of ErPdSb yields: $\rho_0 = 1861.4$ $\mu\Omega$ cm, $n_0 = 0.08$ f.u.$^{-1}$, $N = 2.6$ eV^{-1}, $c_{ph} = 0.23$ $\mu\Omega$ cm K^{-1}, and $E_g = 6$ meV. The obtained parameters are in good agreement with the values reported in Refs. 21 and 22 for similar compounds. The magnitude of the band gap so estimated is about six times smaller then that derived using Eq. (8), and it is only a small fraction of the value of $E_g = 280$ meV calculated from the high-temperature resistivity data.[23] Whereas the latter value represents an intrinsic gap of semiconducting ErPdSb (see the discussion in Ref. 23), the values reported in the present work are due to donor and/or acceptor states located inside the intrinsic gap. Such a conclusion is further supported by the theoretical results: the intrinsic energy gap of about 100 meV has been calculated for a closely related antimonide[31] LuPdSb and gaps in the range 200–500 meV have been derived for the alloys *X*NiSn and *X*NiSb (*X*=Ti, Zr, Hf).[32,33]

2. Thermoelectric power

The temperature dependencies of the thermoelectric power of the two compounds are displayed in Fig. 10. At room temperature the Seebeck coefficient is about 200 μV K^{-1} for YPdSb and 150 μV K^{-1} for ErPdSb. The latter value is considerably smaller than $S = 241$ μV K^{-1} recently reported for this material in Ref. 23. This discrepancy probably arises from a deviation from the ideal stoichiometry

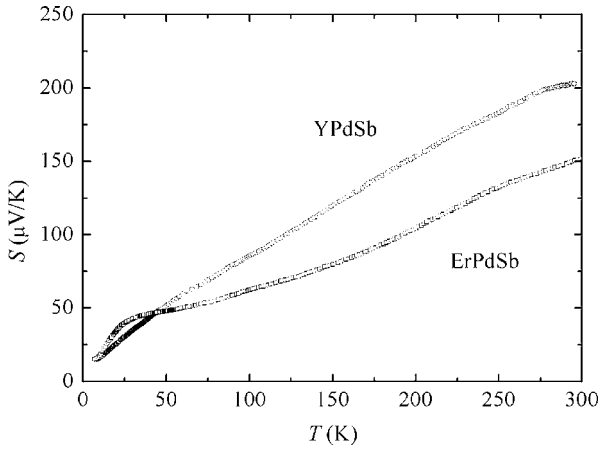

FIG. 10. Temperature dependencies of the thermoelectric power of YPdSb and ErPdSb.

and/or different degree of atomic disorder in the samples studied (note that the room-temperature resistivity of the specimen investigated in Ref. 23 was 5.3 mΩ cm, i.e., much larger compared with ca. 1.8 mΩ cm measured in the present work).

For both YPdSb and ErPdSb, the thermopower is positive in the whole temperature range, which may indicate that hole-type carriers dominate the electrical conduction. The overall temperature dependence of the thermopower is characteristic of low-carrier-density semimetals with parabolic electron and hole bands[34] and is quite similar to $S(T)$ observed for 3*d*-electron-based half-Heusler compounds.[10] In these compounds the Seebeck coefficient is roughly proportional to the temperature in wide temperature ranges, hence indicating that the main contribution to $S(T)$ comes from diffusion of the carriers due to the applied temperature gradient. This mechanism is generally expressed as[35]

$$S(T) = \frac{k_B^2 \pi^2 T}{3eE_F}\left(\frac{\partial \ln n(E)}{\partial \ln E} + \frac{\partial \ln \nu^2(E)}{\partial \ln E} + \frac{\partial \ln \tau(E)}{\partial \ln E}\right), \tag{10}$$

where $n(E)$, $\nu(E)$, and $\tau(E)$ denote the density of states, the velocity of carriers, and the relaxation time of carriers, respectively, near the Fermi level. Within a single-band model with atomic disorder scattering being dominant at high temperatures [i.e., $n(E) \sim E^{1/2}$, $\nu^2(E) \sim E$, and $\tau(E) \sim E^{-1/2}$], the temperature variation of the Seebeck coefficient takes the simple form

$$S(T) = \frac{k_B^2 \pi^2 T}{3eE_F}, \tag{11}$$

The above equation applied to the experimental data of ErPdSb and YPdSb yields the Fermi energy $E_F = 47$ and 32 meV, respectively. These values are considerably smaller than those characterizing simple metals ($E_F \sim 1$–5 eV). The effective carrier concentrations are of the order of 10^{19} cm^{-3} for both compounds, consistent with the high magnitude of their electrical resistivity. For ErPdSb a similar estimate was derived[23] from the high-temperature thermopower and resis-

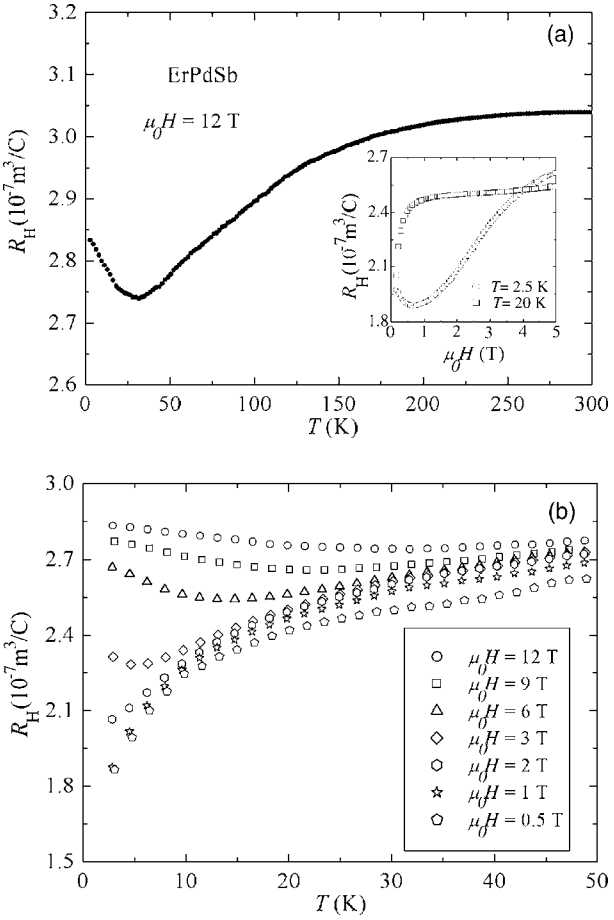

FIG. 11. (a) Temperature dependence of the Hall coefficient for ErPdSb, measured in a magnetic field of 12 T. Inset: Field variation of the Hall coefficient isotherms taken at 2.5 and 20 K. (b) Low-temperature variation of the Hall coefficient measured in several different magnetic fields.

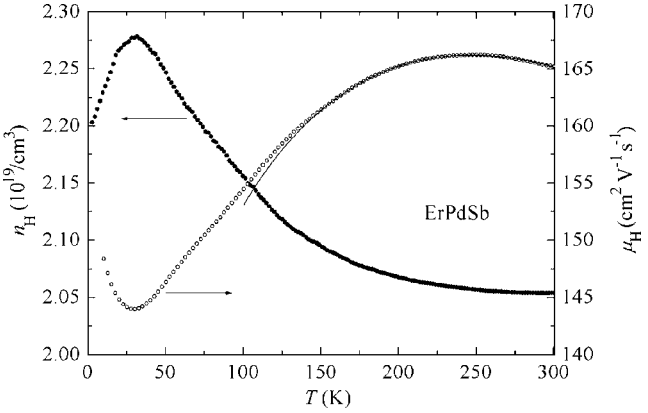

FIG. 12. Temperature dependencies of the Hall carrier concentration (left-hand scale) and the Hall mobility (right-hand scale) for ErPdSb. The solid line represents the least-squares fit of the Hall mobility data to Eq. (12).

tivity data (i.e., from the intrinsic region of electrical conduction). Finally, it should be noted that for ErPdSb a small hump on $S(T)$ is observed near 60 K (see Fig. 10). This anomaly probably results from the phonon drag effect or/and the crystal field effect (as discussed above the first excited CEF state is located ca. 60 K above the ground state).

3. Hall effect

The results of Hall effect measurements of ErPdSb are summarized in Fig. 11. The Hall coefficient measured as a function of temperature in an applied magnetic field of 12 T is positive in the entire temperature range investigated, hence corroborating the conclusion drawn from the thermoelectric data that holes are the majority carriers. In contrast to the case of simple metals, R_H strongly varies with temperature and shows distinct magnetic field dependencies, especially at low temperatures [see the inset to Fig. 11(a) and Fig. 11(b)]. These features indicate a complex underlying electronic structure. Presumably, the concentrations and the mobilities of the carriers, holes and electrons (the latter as minority carriers), exhibit different temperature and magnetic field variations, and hence their particular contributions to the charge transport change with temperature and field. At 300 K the Hall coefficient in ErPdSb amounts to about 3×10^{-7} m^3 C^{-1}. This value is 10^2–10^4 times larger than those typical for simple metals but close to those reported for related semimetallic materials XNiSn (X=Hf,Zr,Ti).[13] With decreasing temperature the Hall coefficient smoothly diminishes down to a temperature $T_{\min}$ at which $R_H(T)$ forms a broad minimum. In 12 T, $T_{\min}$ is about 26 K, and it gradually decreases with decreasing field, becoming smaller than 1.5 K in fields weaker than 2 T. Simultaneously, the minimum in $R_H(T)$ distinctly sharpens [cf. Fig. 11(b)]. These dependencies of the low-temperature Hall effect on the strength of applied magnetic field give rise to different character of the $R_H(B)$ variations measured at 2.5 and 20 K [see the inset to Fig. 11(a)].

Considering a single-band model one may derive the Hall carrier density in ErPdSb, as shown in Fig. 12. The magnitude of n_H is estimated to be of the order of 10^{19} cm^{-3}, in good agreement with the carrier concentration calculated from the thermoelectric power data. Within this simplified approach the temperature dependence of the Hall mobility can also be obtained (see Fig. 12). At 300 K the mobility attains a relatively large value of 165 cm^2 V^{-1} s^{-1}. At lower temperatures $\mu_H(T)$ forms a broad maximum near 250 K and a more distinct minimum at 26 K, yet the magnitude does not change significantly. Assuming that μ_H is limited mainly by ionized impurity and acoustic mode contributions and these two scattering mechanisms satisfy the Matthiessen rule, the temperature variation of the total carrier mobility may be expressed as[36]

$$\mu^{-1}(T) = \mu_{\text{im}}^{-1}(T) + \mu_{\text{ac}}^{-1}(T), \tag{12}$$

where the mobility of charge carriers scattered by ionized impurities is given by $\mu_{\text{im}}=aT^p$ and that due to scattering on acoustic phonons is approximated by $\mu_{\text{ac}}=bT^{-r}$. Here a and b are the transport coefficients, while p and r stand for the scattering parameters, which according to the theory[36] should be close to 3/2. For parabolic spherically symmetric bands the acoustic mobility may be expressed by[37]

$$\mu_{\rm ac} = \frac{(8\pi)^{1/2} e\hbar^4 d_0 \nu^2}{3(k_B T)^{3/2} E_{\rm ac}^2 m_{\rm eff}^{5/2}}, \tag{13}$$

where the velocity of the sound ν is given by $\nu = k_B \Theta_{\rm D}/\hbar \sqrt[3]{6\pi^2 n}$, with n being the number of atoms per unit volume. The parameters d_0, $m_{\rm eff}$, and $E_{\rm ac}$ are the material density, the effective mass of charge carriers, and the acoustic deformation potential, respectively. Taking $\Theta_{\rm D}=270$ K (as derived from the specific heat data) and $n=4.37 \times 10^{28}$ m^{-3} (from the x-ray data) one obtains $\nu = 2575$ m s^{-1}. Setting $d_0=9.564$ g cm^{-3} (from the x-ray data) and assuming $m_{\rm eff}=m_0$ (m_0 is the free electron mass), one may apply Eqs. (12) and (13) to the experimental $\mu(T)$ variation of ErPdSb. The least-squares fit to the data above 120 K, shown by the solid line in Fig. 12, yielded the following parameters: $E_{\rm ac}=1.91$ eV, $a=63.4$ (cm^2 V^{-1} s^{-1} K^{-1})$^{-1}$ and $p=0.19$. The value of $E_{\rm ac}$ so derived is similar to that reported for ZrNiSn single crystals.[38] The deviation of the obtained value of p from the theoretical prediction may be caused by contributions to the mobility from other scattering processes, like optical and piezoacoustic phonon modes. Another reason for the discrepancy could be the limited applicability of the above simplified approach to the low-temperature regime, in which some conductivity contributions coming from the impurity band are not properly considered.

4. Thermal conductivity

The temperature dependence of the thermal conductivity of ErPdSb is shown in Fig. 13. The overall shape of $\kappa(T)$ is similar to the results obtained for other half-Heusler systems.[10] At low temperatures the thermal conductivity sharply increases with increasing temperature, forms a pronounced maximum centered at 50 K, and then decreases moderately showing a tendency to saturate above ca. 200 K. The thermal conductivity measured at room temperature is 3.3 W m^{-1} K^{-1}, which is a smaller value than that recently reported in Ref. 23 ($\kappa \approx 5$ W m^{-1} K^{-1}, calculated from the thermodynamic data at 300 K). The maximum in $\kappa(T)$ occurs due to reduction of the thermal scattering at low temperatures, i.e., in the regime where the phonon mean free path becomes larger than the interatomic distances.

In general, the total thermal conductivity of nonmagnetic metals and semimetals is usually expressed as a sum of the electronic κ_e and lattice κ_L terms. The electronic contribution can be estimated using the Wiedemann-Franz law, $\kappa_e = L_0/\rho$, where L_0 is the Lorenz constant ($L_0=2.45\times10^{-8}$ W Ω K^{-2}) and ρ stands for the electrical resistivity. The $\kappa_e(T)$ so derived for ErPdSb is displayed in Fig. 13 as the dotted line. Apparently, the charge carrier scattering brings about just a small contribution to the total thermal transport, which is dominated by the phonon term, especially at low temperatures. According to the Callaway model,[39–41] i.e., within the Debye approximation for the phonon spectrum, the lattice thermal conductivity can be written as

$$\kappa_L = \frac{k_B}{2\pi^2 \nu}\left(\frac{k_B T}{\hbar}\right)\int_0^{\Theta_D/T} \frac{\tau_p x^4 e^x}{(e^x-1)^2} dx, \tag{14}$$

where ν is the velocity of sound, τ_p stands for the relaxation time, $x=\hbar\omega/k_B T$, ω is the phonon frequency, and n is the

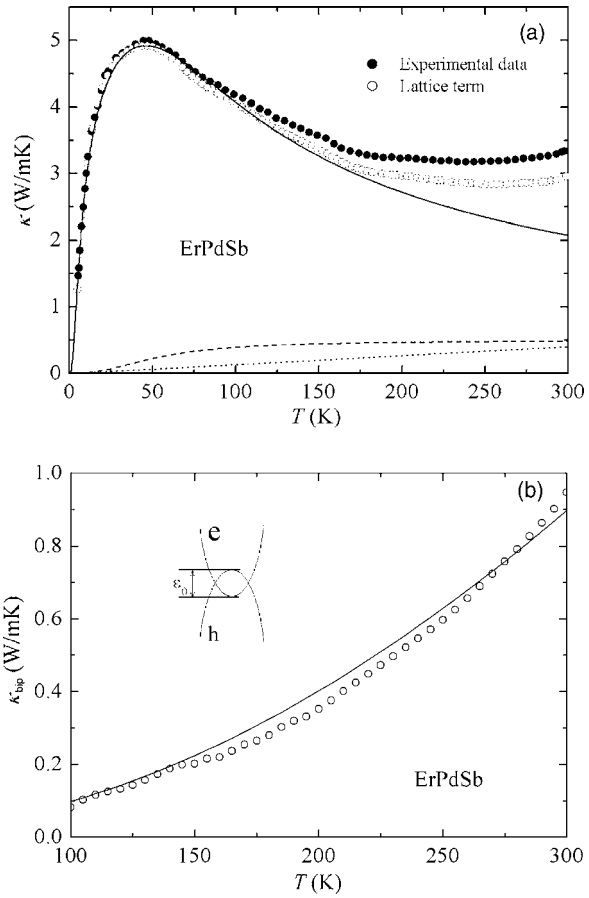

FIG. 13. (a) Temperature dependence of the thermal conductivity of ErPdSb (full circles). The dotted curve is the estimated electronic contribution and the open circles represent the lattice conductivity data. The solid line is the least-squares fit of the lattice term to Eq. (14). The dashed curve presents the minimal phonon thermal conductivity calculated from Eq. (19). (b) Temperature dependence of the bipolaron contribution to the total thermal conductivity of ErPdSb (the scheme shows electron e and hole h bands overlapping by energy ε_0). The open circles represent here the excess experimental thermal conductivity (see the text) and the solid curve is the calculated bipolaron term.

number of atoms per unit volume, while $\hbar$, Θ_D, and k_B are the reduced Planck constant, Debye temperature, and the Boltzmann constant, respectively. In turn, the relaxation time may be accounted for by considering possible different mechanisms of the heat transport: point defect scattering, boundary scattering, umklapp processes, and scattering of phonons by electrons

$$\tau_p^{-1} = \tau_D^{-1} + \tau_B^{-1} + \tau_U^{-1} + \tau_{\rm ph\text{-}el}^{-1}, \tag{15}$$

where the particular inverse relaxation times are given by the following expressions:

$$\tau_D^{-1} = Dx^4 T^4, \quad \tau_B^{-1} = B, \quad \tau_U^{-1} = UT^3 x^2 e^{-\Theta_D/2T}, \quad \tau_{\rm ph\text{-}el}^{-1} = ETx. \tag{16}$$

With the sound velocity $\nu=2575$ m s^{-1}, as calculated above, the experimental $\kappa_L(T)$ variation can be well fitted by Eq. (14) below 175 K, as shown by the solid line in Fig. 13.

The relative weight parameters obtained for the different phonon scattering processes are $D=7.63\times10^4$ K^{-4} s^{-1}, $B=4.92\times10^9$ s^{-1}, $U=10.1\times10^5$ K^{-3} s^{-1}, and $E=2.54\times10^4$ K^{-1} s^{-1}, respectively. The grain boundary scattering is dominant at low temperatures, while the umklapp scattering is important at high temperatures. Besides these two mechanisms, the position of the maximum in $\kappa_L(T)$ and its characteristic shape are mainly governed by the point defect scattering.

At temperatures above about 175 K, one observes a pronounced deviation of the experimental data from the theoretical curve. This discrepancy probably arises due to radiation losses, usually perturbing at high temperatures the steady-state measurements of the thermal conductivity. Other reasons might be possible error in the input value of the Debye temperature or/and the oversimplified assumption that the Lorenz number is independent of the temperature. However, the observed behavior could also be caused by intrinsic physical mechanisms neglected in the analysis, like a bipolaron contribution which is frequently observed in semimetallic systems.[42] Assuming that holes and electrons are scattered independently with the relaxation time $\tau\sim E^r$, and the hole and electron bands have parabolic shapes, the thermal conductivity due to bipolarons κ_{bip} may be expressed as[43]

$$\kappa_{\text{bip}} = T\left(\frac{k_B}{e}\right)^2\left[\frac{A_e}{\rho_e}+\frac{A_h}{\rho_h}+\frac{1}{\rho_e+\rho_h}\left(\delta_e+\delta_h-\frac{\varepsilon_0}{k_BT}\right)^2\right], \tag{17}$$

where ρ_e and ρ_h are the electrical resistivities due to electrons and holes, respectively, $\delta_{e,h}$ and $A_{e,h}$ are the parameters describing the scattering processes of the two types of carriers, whereas ε_0 denotes the overlapping energy of the electron and hole bands [see Fig. 13(b)]. With the additional assumption that both types of carriers are scattered similarly, i.e., $\rho_e=\rho_h$, $\delta_e=\delta_h$, $A_e=A_h=A$, and mainly the acoustic phonons are involved, i.e., $r=-\frac{1}{2}$, the above equation transforms into the formula[43]

$$\frac{\kappa_{\text{bip}}}{\kappa_e} = \frac{(\delta-\varepsilon_0/2k_BT)^2}{A}. \tag{18}$$

Figure 13(b) shows the excess thermal conductivity over the electronic term and the lattice contribution derived from Eq. (14), together with the bipolaron term calculated from Eq. (18) for $\varepsilon_0=23$ meV. The good agreement between the experimental data and $\kappa_{\text{bip}}(T)$ may suggest that indeed the bipolaron scattering plays an important role in the thermal transport in ErPdSb. However, further experimental studies, e.g., optical spectroscopy, are required to verify this hypothesis.

E. Thermoelectric performance

Large values of the Seebeck coefficient together with relatively small electrical resistivities observed in ErPdSb and YPdSb lead to high values of the thermoelectric power factor $\mathcal{F}=S^2/\rho$ which is the main prerequisite for good thermoelectrical efficiency. Figure 14 displays the temperature dependencies of $\mathcal{F}$ of the two compounds studied. For both materials the power factor increases with rising temperature and at 300 K it achieves rather large values: $\mathcal{F}=12$ μW cm^{-1} K^{-2} for ErPdSb and 3 μW cm^{-1} K^{-2} for YPdSb. These values are similar to those previously observed for stannides from the XNiSn (X=Ti, Hf, Zr) system.[15]

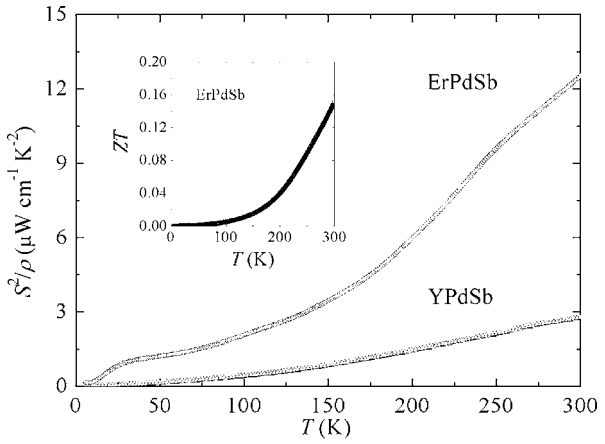

FIG. 14. Temperature dependence of the thermoelectric power factor of ErPdSb and YPdSb. Inset: Temperature variation of the figure of merit for ErPdSb.

The high magnitude of $\mathcal{F}$ derived for ErPdSb together with the relatively small thermal conductivity lead to a dimensionless figure of merit $ZT=S^2T/\rho\kappa$ of about 0.15 at room temperature (see the inset to Fig. 14). This value of ZT is similar to those found for doped 3d-electron transition-metal-based half-Heusler phases,[19] and "rattling" systems like skutterudites and clathrates,[44,45] which are all currently intensively investigated in a field of possible applications as novel thermoelectrics. It is, however, smaller than those characterizing state-of-the-art bulk thermoelectric materials.[46] Though above room temperature the figure of merit of ErPdSb continues to increase, it does not exceed 0.17, which is observed at about 700 K.[23]

In the context of the thermoelectrical performance of ErPdSb it is worthwhile comparing the measured lattice thermal conductivity of ErPdSb with the theoretically achievable minimal magnitude of the phonon contribution. The latter may be calculated from the expression:[47,48]

$$\kappa_{L_{\text{min}}} = \left(\frac{3n}{4\pi}\right)^{1/3}\frac{k_B^2T^2}{\hbar\theta_D}\int_0^{\Theta_D/T}\frac{x^3e^x}{(e^x-1)^2}dx, \tag{19}$$

in which no distinction is made between the transverse and longitudinal acoustic phonon modes. The result obtained for ErPdSb ($\Theta_D=270$ K and $n=4.37\times10^{28}$ m^{-3}) is shown in Fig. 13 by the dashed line. Clearly, $\kappa_{L_{\text{min}}}$ is much smaller than the measured κ_L in the entire temperature range, thus indicating the possibility of increasing ZT by lowering the thermal conductivity. It may be achieved, e.g., by increasing the magnitude of atomic disorder. In the case of skutterudites and clathrates,[49,50] the mean free path of phonons becomes very short due to scattering on rattling "guest" atoms. Similarly, in strongly atomically disordered materials the mean free path of phonons is short because of scattering by atomic

disorder. In such materials the lattice thermal conductivity measured at high temperatures closely approaches $\kappa_{L_{\min}}$.

IV. SUMMARY AND CONCLUSION

Magnetic susceptibility measurements of the half-Heusler phases ErPdSb and YPdSb revealed that the Er-based compound is a Curie-Weiss paramagnet due to the presence of R^{3+} ions, while YPdSb is a weak diamagnet. From the specific heat data, the crystal field splitting of the Er^{3+} ground multiplet was estimated to be about 186 K, with a doublet being the crystal field ground state, and a quartet and a doublet being the nearest excited states. Both compounds were found to exhibit semimetallic or narrow-gap semiconducting behavior.[30] The electrical resistivity of ErPdSb shows a metalliclike behavior at low temperatures and activated behavior at high temperatures. In turn, the electrical resistivity of YPdSb exhibits semiconductinglike character in the whole temperature range studied. The energy gaps at the Fermi level were estimated to be of the order of 10^{-2} eV in both compounds. In general, all these findings agree well with the recently published results on the high-temperature electrical transport in ErPdSb (Ref. 23) and YPdSb,[51] which is clearly driven by the formation of narrow gaps in the electronic band structure near the Fermi energy. The values of the energy gaps derived from the low-temperature data are, however, smaller than those obtained via the high-temperature experiments.[23,51] They are also much smaller than the values calculated for similar alloys.[31–33] Thus, these gaps should be associated with the in-gap states rather than with the intrinsic conductivity regime.

The Seebeck coefficient is a sensitive probe of electronic band structure close to the Fermi level. For both compounds studied, the sign of the Seebeck coefficient is positive in the entire temperature range, which indicates that holes are dominant carriers. For ErPdSb the Hall effect measurements corroborated the semimetallic character of the electrical conductivity with holes being the majority carriers. The *p*-type conductivity is probably due to the presence of some acceptor levels at energies just above the valence band, created by atomic disorder. The estimated carrier concentration is of the order of 10^{19} cm^{-3}, in good agreement with the thermoelectric data. The large thermopower together with the optimal carrier concentration make ErPdSb and YPdSb promising candidates for thermoelectric applications.[52] The rather low thermal conductivity in the Er-based compound, in concert with suitable charge transport characteristics, yields the thermoelectric figure of merit $ZT \sim 0.15$ at room temperature. This relatively large ZT may be a good starting point for optimization of the thermoelectrical performance by means of intentional reduction of the phonon thermal conductivity. This challenge may be accomplished, for example, by controlled doping (alloying) of the host lattice or/and by increasing the level of structural disorder by appropriate heat treatment.

ACKNOWLEDGMENTS

The authors thank Ulrich Burkhardt for metallographic analyses of the investigated samples. K.G. and D.K. are indebted to the Max-Planck-Society for financial support.

[1] J. Pierre, R. V. Skolozdra, J. Tobola, C. Hordequin, M. A. Kouacou, I. Karla, R. Currat, and E. Lelievere-Berna, J. Alloys Compd. **262-263**, 101 (1997).
[2] P. C. Canfield, J. D. Thompson, W. P. Beyermann, A. Lacerda, M. F. Hundley, E. Petersen, and Z. Fisk, J. Appl. Phys. **70**, 5800 (1991).
[3] M. F. Hundley, J. D. Thompson, P. C. Canfield, and Z. Fisk, Phys. Rev. B **56**, 8098 (1997).
[4] A. Szytuła, A. Jezierski, B. Penc, A. Winiarski, A. Leithe-Jasper, and D. Kaczorowski, J. Alloys Compd. **360**, 41 (2003).
[5] D. Kaczorowski, A. Leithe-Jasper, P. Rogl, H. Flandorfer, T. Cichorek, R. Pietri, and B. Andraka, Phys. Rev. B **60**, 422 (1999).
[6] T. J. Zhu, L. Lu, M. O. Lai, and J. Ding, Smart Mater. Struct. **14**, S293 (2005).
[7] J. Pierre and I. Karla, J. Magn. Magn. Mater. **217**, 74 (2000).
[8] I. Karla, J. Pierre, and R. V. Skolozdra, J. Alloys Compd. **265**, 42 (1998).
[9] R. A. de Groot, F. M. Mueller, P. G. van Engen, and K. H. J. Buschow, Phys. Rev. Lett. **50**, 2024 (1983).
[10] C. Uher, J. Yang, S. Hu, D. T. Morelli, and G. P. Meisner, Phys. Rev. B **59**, 8615 (1999).
[11] F. G. Aliev, N. B. Brandt, V. V. Moshchalkov, V. V. Kozyrkov, R. V. Skolozdra, and A. I. Belogorokhov, Z. Phys. B: Condens. Matter **75**, 167 (1989).
[12] F. G. Aliev, V. V. Kozyrkov, V. V. Moshchalkov, R. V. Skolozdra, and K. Durczewski, Z. Phys. B: Condens. Matter **80**, 353 (1990).
[13] F. G. Aliev, Physica B **171**, 199 (1991).
[14] B. A. Cook and J. L. Harringa, J. Mater. Sci. **34**, 323 (1999).
[15] H. Hohl, A. P. Ramirez, C. Goldmann, G. Ernst, B. Wölfing, and E. Bucher, J. Phys.: Condens. Matter **11**, 1697 (1999).
[16] Y. Xia, S. Bhattacharya, V. Ponnambalam, A. L. Pope, S. J. Poon, and T. M. Tritt, J. Appl. Phys. **88**, 1952 (2000).
[17] S. Bhattacharya, A. L. Pope, R. T. Littleton, T. M. Tritt, V. Ponnambalam, Y. Xia, and S. J. Poon, Appl. Phys. Lett. **77**, 2476 (2000).
[18] Q. Shen and L. Zhang, J. Mater. Sci. **20**, 2197 (2001).
[19] Q. Shen, L. Chen, T. Goto, T. Hirai, J. Yang, G. P. Meisner, and C. Uher, Appl. Phys. Lett. **79**, 4165 (2001).
[20] Y. Kawaharada, H. Uneda, H. Muta, K. Kurosaki, and S. Yamanaka, J. Alloys Compd. **364**, 59 (2004).
[21] D. Kaczorowski, K. Gofryk, T. Plackowski, A. Leithe-Jasper, and Yu. Grin, J. Magn. Magn. Mater. **290-291**, 573 (2005).
[22] K. Gofryk, D. Kaczorowski, T. Plackowski, A. Leithe-Jasper, and Yu. Grin, Phys. Rev. B **72**, 094409 (2005).
[23] T. Sekimoto, K. Kurosaki, H. Muta, and S. Yamanaka, J. Appl. Phys. **99**, 103701 (2006).
[24] A. Jeżowski, J. Mucha, and G. Pompe, J. Phys. D **20**, 1500 (1987).

[25] S. K. Malik and D. T. Adroja, J. Magn. Magn. Mater. **102**, 42 (1991).
[26] G. L. F. Fraga and D. E. Brandão, J. Magn. Magn. Mater. **102**, 199 (1991).
[27] A. Tari, *The Specific Heat of Matter at Low Temperatures* (Imperial College Press, London, 2003).
[28] K. R. Lea, M. J. M. Leask, and W. P. Wolf, J. Phys. Chem. Solids **23**, 1381 (1962).
[29] I. Karla, J. Pierre, A. P. Murani, and M. Neumann, Physica B **271**, 294 (1999).
[30] R. Dornhaus, G. Nimitz, and B. Schlicht, *Narrow-Gap Semiconductors* (Springer, Berlin, 1983).
[31] K. Mastronardi, D. Young, C. C. Wang, P. Khalifah, R. J. Cava, and A. P. Ramirez, Appl. Phys. Lett. **74**, 141 (1999).
[32] S. Öğüt and K. M. Rabe, Phys. Rev. B **51**, 10443 (1995).
[33] P. Larson, S. D. Mahanti, S. Sportouch, and M. G. Kanatzidis, Phys. Rev. B **59**, 15660 (1999).
[34] K. Durczewski and M. Ausloos, Z. Phys. B: Condens. Matter **85**, 59 (1991).
[35] R. D. Bernard, *Thermoelectricity in Metals and Alloys* (Taylor and Francis, London, 1972).
[36] D. L. Rode, in *Semiconductors and Semimetals*, edited by R. K. Willardson and A. C. Beer (Academic Press, New York, 1975), Vol. 10, pp. 1–89.
[37] J. Bardeen and W. Shockley, Phys. Rev. **77**, 407 (1950).
[38] E. Arushanov, W. Kaefer, K. Fess, Ch. Kloc, K. Friemelt, and E. Bucher, Phys. Status Solidi A **177**, 511 (2000).
[39] J. Callaway, Phys. Rev. **113**, 1046 (1959).
[40] J. Callaway and H. C. von Baeyer, Phys. Rev. **120**, 1149 (1960).
[41] J. Callaway, Phys. Rev. **122**, 787 (1961).
[42] A. V. Golubkov, L. S. Parfen'eva, I. A. Smirnov, H. Misiorek, J. Mucha, and A. Jeżowski, Phys. Solid State **42**, 1394 (2000).
[43] I. A. Smirnov and V. I. Tamarchenko, *Electronic Thermal Conduction in Metals and Semiconductors* (Nauka, Leningrad, 1977).
[44] E. A. Skrabek, D. S. Trimmer, and G. A. Slack, in *CRC Handbook of Thermoelectrics*, edited by D. M. Rowe (CRC Press, Boca Raton, FL, 1995).
[45] N. P. Blake, L. Møllnitz, G. Kresse, and H. Metiu, J. Chem. Phys. **111**, 3133 (1999).
[46] T. M. Tritt, *Encyclopedia of Materials: Science and Technology* (Elsevier Science, Amsterdam, 2002).
[47] K. Gianno, A. V. Sologubenko, M. A. Chernikov, H. R. Ott, I. R. Fisher, and P. C. Canfield, Phys. Rev. B **62**, 292 (2000).
[48] D. G. Cahill and R. O. Pohl, Solid State Commun. **70**, 927 (1989).
[49] B. C. Sales, D. Mandrus, B. C. Chakoumakos, V. Keppens, and J. R. Thompson, Phys. Rev. B **56**, 15081 (1997).
[50] J. L. Cohn, G. S. Nolas, V. Fessatidis, T. H. Metcalf, and G. A. Slack, Phys. Rev. Lett. **82**, 779 (1999).
[51] J. Oestreich, U. Probst, F. Richardt and E. Bucher, J. Phys.: Condens. Matter **15**, 635 (2003).
[52] G. D. Mahan, *Good Thermoelectrics*, Solid State Physics—Advances in Research and Applications Vol. 51, edited by H. Ehrenreich and F. Saepen (Academic Press, San Diego, 1997).